PAPER

Triangular nanoperforation and band engineering of InGaAs quantum wells: a lithographic route toward Dirac cones in III–V semiconductors

To cite this article: L C Post *et al* 2019 *Nanotechnology* **30** 155301

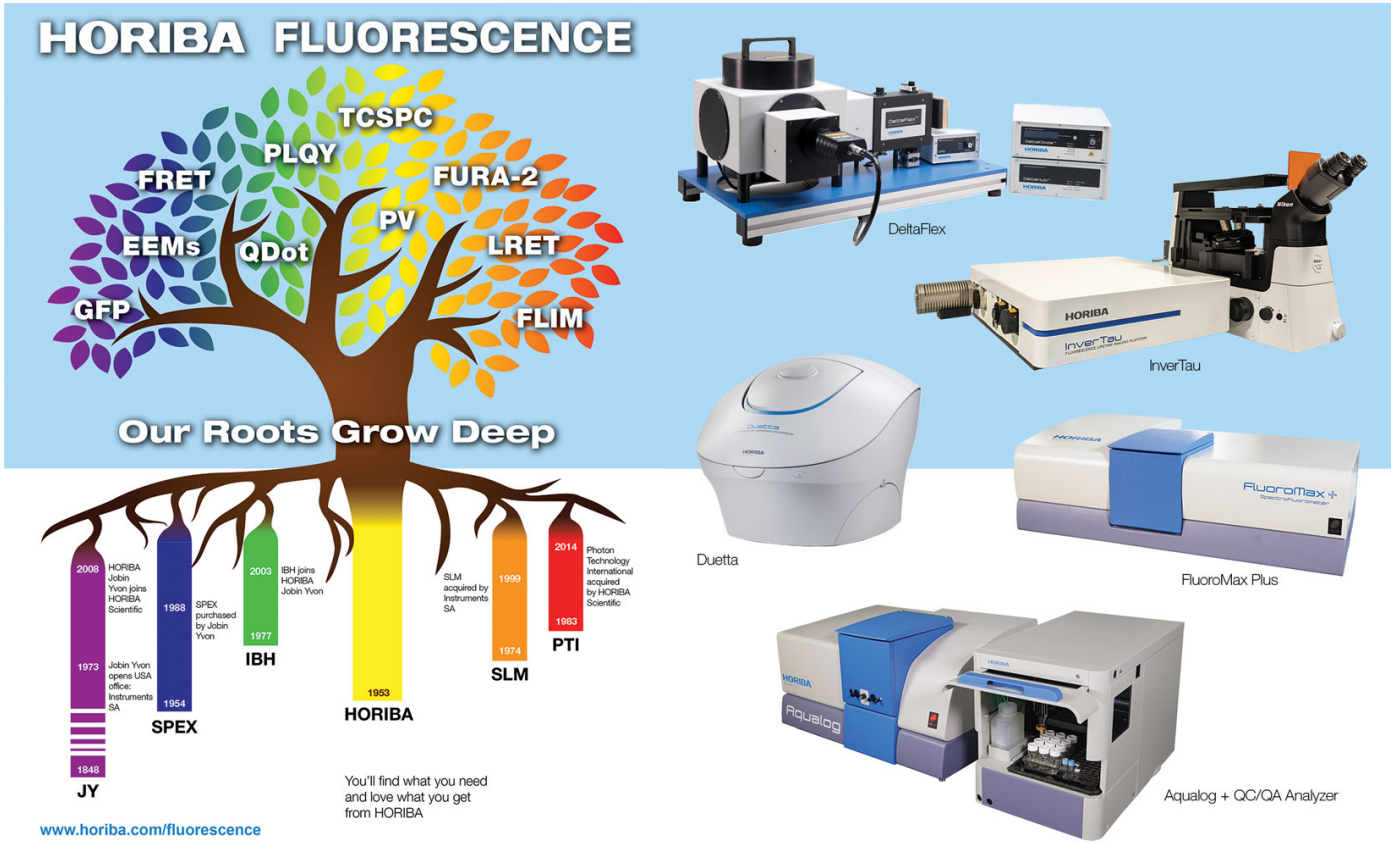

IOP Publishing Nanotechnology
Nanotechnology 30 (2019) 155301 (10pp) https://doi.org/10.1088/1361-6528/aafd3f

Triangular nanoperforation and band engineering of InGaAs quantum wells: a lithographic route toward Dirac cones in III–V semiconductors

L C Post[1], T Xu[2,3,4], N A Franchina Vergel[2], A Tadjine[2], Y Lambert[2], F Vaurette[2], D Yarekha[2], L Desplanque[2], D Stiévenard[2], X Wallart[2], B Grandidier[2], C Delerue[2] and D Vanmaekelbergh[1,4]

[1] Condensed Matter and Interfaces, Debye Institute for Nanomaterials Science, Utrecht University, 3584 CC Utrecht, The Netherlands
[2] IEMN, UMR8520, Université de Lille1, F-59652 Villeneuve d'Ascq Cédex, France
[3] Key Laboratory of Advanced Display and System Applications, Shanghai University, 200072 Shanghai, People's Republic of China

E-mail: xtld@shu.edu.cn and d.vanmaekelbergh@uu.nl

Received 27 September 2018, revised 6 December 2018
Accepted for publication 10 January 2019
Published 8 February 2019

Abstract

The design of two-dimensional periodic structures at the nanoscale has renewed attention for band structure engineering. Here, we investigate the nanoperforation of InGaAs quantum wells epitaxially grown on InP substrates using high-resolution e-beam lithography and highly plasma based dry etching. We report on the fabrication of a honeycomb structure with an effective lattice constant down to 23 nm by realising triangular antidot lattice with an ultimate periodicity of 40 nm in a 10 nm thick InGaAs quantum well on a p-type InP. The quality of the honeycomb structures is discussed in detail, and calculations show the possibility to measure Dirac physics in these type of samples. Based on the statistical analysis of the fluctuations in pore size and periodicity, calculations of the band structure are performed to assess the robustness of the Dirac cones with respect to distortions of the honeycomb lattice.

Supplementary material for this article is available online

Keywords: InGaAs quantum well, honeycomb semiconductor, dirac cone, electron beam lithography, band structure engineering, lattice disorder

(Some figures may appear in colour only in the online journal)

1. Introduction

III–V semiconductor quantum wells have obtained a central place in opto-electronics and advanced logics. In more recent quests for semiconductors with entirely new functions, the effects of a periodic potential at the nanometre scale on the electronic band structure have been theoretically anticipated [1, 2]. In the case where the charge carriers are confined in a honeycomb geometry, the quantum well semiconductor bandgap remained, but the highest hole valence and lowest electron conduction bands become Dirac cones with a linear energy-momentum relationship around the K-points in the Brillouin zone. This means that the beneficial properties of a semiconductor, such as a bandgap and a controllable density of carriers, can be combined with valence and conduction bands with a K-region similar as for graphene. Moreover, the combination of Dirac (mini) bands and spin–orbit coupling may result in topological phases, such as non-trivial flat bands

[4] Authors to whom any correspondence should be addressed.

and the quantum spin Hall effect [3–6]. Hence, honeycomb semiconductors (HC-SC) form a new material class with unseen electronic functions.

With respect to the question of how to fabricate such HC-SC, two possibilities have been put forward, recently. The first route is based on the two-dimensional (2D) assembly and attachment of semiconductor nanocrystals providing HC-SC of Pb- and Cd-chalcogenides [7, 8] with a periodicity in the 5–10 nm range, supported by calculations [3, 9]. The second route is based on nanopatterning of 2D semiconductors by means of lithography. Importantly, a hexagonal array of pores in a semiconductor quantum well would result in a remaining crystal with a honeycomb geometry.

Such a lithographic nanoperforation to form HC-SC has several advantages: (i) it can be applied to families of well-established semiconductor materials with low effective carrier mass and very high electron mobilities, such as several III–V semiconductors; (ii) nanoperforation would enable to change the size of the honeycomb unit cell and the size of the pores in an independent way. This allows for a precise tuning of the electronic band structure. (iii) The lithographic procedures can be directly applied to semiconductor quantum wells incorporated in classic transistor devices, allowing for direct investigation of the band structure and transport properties of the HC-SC with a controllable position of the Fermi-level.

Previous works used a modulation-doped GaAs heterostructure subjected to a lateral attractive potential with honeycomb geometry [10–13]. Experiments revealed interesting many-body effects but direct evidence for massless Dirac fermions (MDFs) remains elusive because the width of the Dirac band was too small ($\ll$0.1 meV) due to the relatively large lattice constant ($>$100 nm) [14]. Recently, Wang *et al* realised a HC-SC in a nanopatterned GaAs quantum well with a very small lattice constant of 50 nm. Resonant inelastic light-scattering spectra revealed some features of Dirac type bands [15]. However, it was reported that the lattice parameter of HC-SC based on GaAs heterostructures should be as low as 20 nm to directly observe MDFs in standard cryogenic conditions [2]. As a result, nanofabrication techniques should be pushed to their ultimate limit in terms of resolution. We note that it is more effective to etch a triangular antidot lattice with a repulsive potential, than using an attractive potential. With this approach, the lattice constant of the honeycomb unit cell can be decreased by a factor $\sqrt{3}$ compared with previous results, which will significantly increase the width of the Dirac band [16].

Devices with remote metallic gates have been commonly used in the previous works. Nevertheless, the potential modulation induced by the top and back gates is necessarily slowly varying in space due to the long-range decay of the Coulomb potentials. In addition, these nanostructures are not suitable for local-probe spectroscopy experiments due to the presence of the top gate. In this work, we have considered another approach allowing to create potential barriers directly in an InGaAs quantum well with steepest variations and thus better definition of the honeycomb lattice.

The width of the Dirac cone is not only dependent on the lattice constant of the honeycomb lattice, but also on the effective mass of the charge carriers in the employed semiconductor material [12]. When lowering the effective mass of the semiconductor material, the effects of the lateral confinement are enhanced, resulting in a broader Dirac cone. Calculations from Tadjine *et al* show that the energy range of the Dirac cone can extend over tens of meV in HC-SC with a reasonable size of lattice parameters in InAs heterostructures [1]. In-based semiconductor materials are therefore promising candidates as 2DEG channel materials for realising Dirac semiconductors. For instance, InGaAs with a relatively low electron effective mass (0.041 m_0 for $In_{0.53}Ga_{0.47}As$ lattice-matched to InP), can be grown by molecular beam epitaxy (MBE) on InP substrates using well-established routes, leading to 2DEG with high carrier mobility ($>1.3 \times 10^5$ cm^2 V^{-1} s^{-1} at 77 K) [17–20]. Finally, another important factor which is usually not considered is the quality of the build-in honeycomb symmetry etched in the QW. Positional disorder in the antidot lattice can greatly affect the symmetry in the lattice, perturbating the Dirac cone and providing mass to the carriers [21]. The fabrication of high quality antidot triangular lattices is essential for the observation of Dirac physics in these samples.

In the present work, we describe a lithographic nanoperforation route towards honeycomb InGaAs on an InP substrate. We describe how a hexagonal array of pores (antidot lattice) is perforated to force the electrons in a honeycomb geometry. The 2D InGaAs layer has a thickness of 10 nm, and is grown on an InP substrate by MBE. Using high-resolution electron beam lithography (EBL) and plasma based dry etching, a triangular antidot lattice is obtained in the InGaAs quantum well with a periodicity of 40 nm which gives an effective honeycomb lattice constant down to 23 nm. We show that the radius of the pores can be tuned in an independent way. Our band structure calculations anticipate that Dirac cones can be obtained with a width of 5.0 meV, allowing for electrical spectroscopy and transport measurements at liquid helium temperature. The morphology of the samples was studied with atomic force microscopy (AFM), energy dispersive electron spectroscopy (EDS) and cross-section transmission electron microscopy (TEM). The disorder in the lattices is quantified on the basis of scanning electron microscopy (SEM) images. We estimate the electronic effects of structural disorder on the density of states (DOS) in the fabricated honeycomb InGaAs structures using a muffin-tin calculation.

2. Experimental

2.1. Sample fabrication

Figure 1 illustrates the fabrication process of the InGaAs antidot lattices. An $In_{0.53}Ga_{0.47}As$ layer (10 nm) was grown onto the InP substrate using MBE. To protect the surface of the QW layer from carbon contaminations, 16 nm of SiO_2 was grown on top of the QW using plasma-enhanced chemical vapour deposition, presented in figure 1(a). The sample

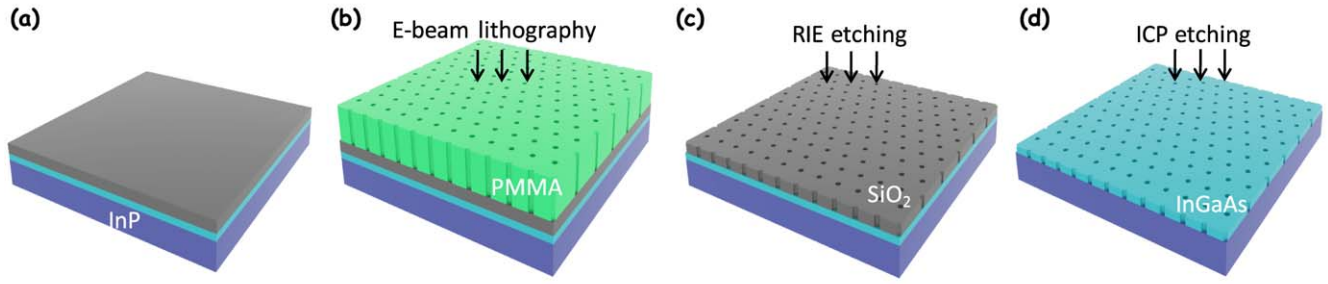

Figure 1. Overview of the fabrication process required to obtain a nanoperforated InGaAs/InP heterostructure with a honeycomb lattice. (a) The starting point is a 10 nm InGaAs quantum well grown with MBE on an InP substrate, on which a SiO_2 layer (16 nm in thickness) and a PMMA layer are deposited. (b) A triangular pattern of pores is created in the PMMA by electron beam lithography, (c) the triangular pattern is transferred into the SiO_2 layer by reactive ion etching. (d) The triangular pore pattern is transferred into the InGaAs quantum well by BCl_3 based inductive coupled plasma etching.

was dehydrated by heating the surface to 180 °C for 10 mins and a diluted polymethylmethacrylate (PMMA) 950 K 4% resist with a thickness of 50 nm was spin-coated on top of the sample, followed by an annealing step at 80 °C for 1 min on a hot plate and a bake out at 180 °C for 10 min.

E-beam exposure was performed using Raith EBPG 5000Plus equipment, taking advantage of the improved recipes of our previous work [22]. Triangular nanopatterns with different periodicities of 60, 50 and 40 nm were exposed in 20 × 5 μm^2 areas with an accelerating voltage of 100 kV, a beam current of 200 pA and an e-beam dose of 10 000 $\mu C\,cm^{-2}$. By slowly modulating the electron beam dose and the aperture in the lithography process, triangular lattices with nanoscale dimensions can be obtained. Since the array fabrication is near the lithography resolution, an additional degree of freedom consists in varying the electron beam dose to slightly change the radius of the pores. The position of the patterns on the sample can be located by printing large markers around the patterns. The resist was developed in a 1:2 methyl-isobutyl ketone:isopropanol (MIBK:IPA) solution for 60 s, removing the exposed resist. The sample was further rinsed in IPA for at least 30 s to stop the development and dried under low N_2 flow (figure 1(b)).

The triangular pattern was first etched inside the SiO_2 layer using reactive ion etching (RIE) in a Plasmalab 80+ (Oxford) system with a mixture of CHF_3 and CF_4 (figure 1(c)). The chamber pressure was set to 10 mTorr, while the power was 300 W. The sample was etched for 40 s, removing all the SiO_2 inside the pores. The remaining PMMA resist on top of the SiO_2 was removed by placing the sample in a SVC bath at 70 °C (2 mins), followed by an acetone bath (2 mins) and finally a IPA bath (2 mins). The sample was further rinsed with IPA and low N_2 flow.

In the final step, the triangular pattern was etched inside the InGaAs QW using BCl_3 based inductively coupled plasma (ICP) etching with a ICP power of 200 W and a RIE power of 50 W. The pressure inside the chamber is set to 2 mTorr and the sample is etched for 40 s, removing the InGaAs inside the pores. The advantage of using ICP etching over conventional RIE is the seperate control over the generated plasma density and the accelerating ion energy, allowing for a better selectivity on the etched sample [23]. The remainder of SiO_2 mask on the sample was removed by wet etching (1% HF for 1 min). The final result of the whole fabrication process is presented in figure 1(d).

2.2. Characterisation

SEM images of the etched SiO_2 and InGaAs layers are shown in figure 2. The left three images (a1, a2, a3) show the triangular antidot array of the 16 nm SiO_2 layer after the first etching step in the patterning process. The triangular pore arrays have a lattice constant of 60, 50 and 40 nm, respectively. The triangular arrays in the InGaAs QW with the same lattice parameters are presented in the right three SEM images (b1, b2, b3) after the ICP etching. Differences in intensity at the edges of the pores can be explained by an accumulation of electrons around the pores.

Over large areas of 20 × 5 μm^2, a uniform pore radius and periodicity can be achieved after optimising the EBL and etching process, with very few pore defects such as missing or misplaced sites. The ability to fabricate the high quality triangular pores with periodicity of 40 nm which gives an effective honeycomb lattice constant of 23 nm ($40/\sqrt{3}$), is essential for optimal tuning of the triangular potential that generates the honeycomb geometry inside the QW with a periodicity of 23 nm.

AFM measurements were performed on the etched samples to check the height profile of the pores and alignment markers (figure 3). Figure 3(a) shows that 18 nm of the substrate sample has been etched in the marker, indicating that the InGaAs QW with initial thickness of 10 nm is completely removed. These results are supported by EDS measurements: on the non-etched area (square 1 of figure 3(a)), Ga and As are found, consistent with the top InGaAs layer, while on the etched area (square 2 of figure 3(a)), these peaks are absent, demonstrating the complete etching of the InGaAs QW. The spectrum acquired on the QW also shows that the remaining SiO_2 on the QW is removed using the wet etching, since no Si peaks are visible and the amplitude of the O peak is similar to the one observed on the InP substrate.

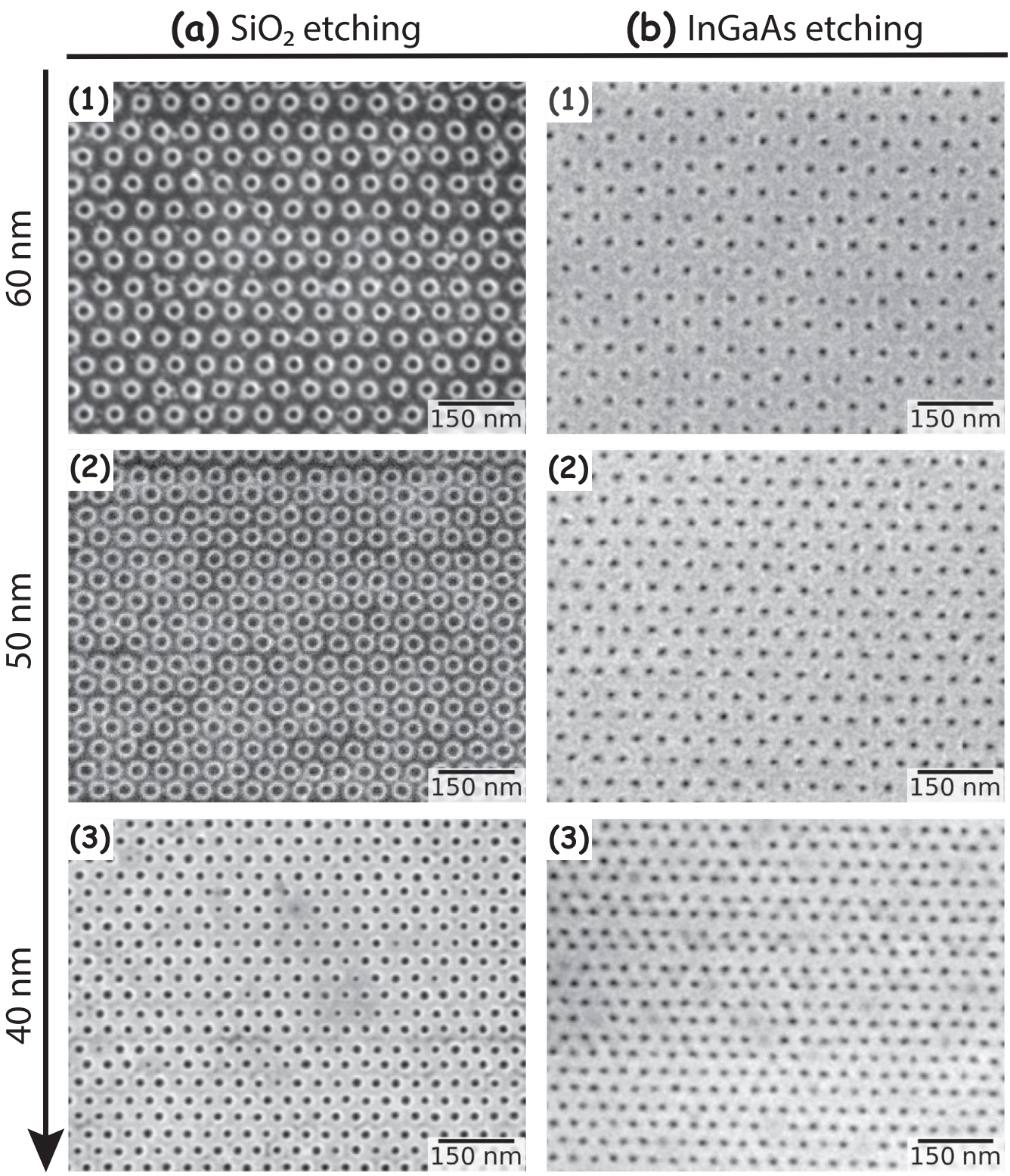

Figure 2. Results of the lithographic patterning in every intermediate stage of the process. (a) SEM images of the triangular pore pattern in the SiO_2 layer after RIE etching. The periodicities of the lattices are 60 (1), 50 (2) and 40 nm (3) in the top, middle, and bottom image, respectively. Differences in intensity at the edges of the pores can be explained by an accumulation of electrons around the pores. (b) SEM images of the pore pattern in the InGaAs quantum well layer after the ICP etching step for 60 (1), 50 (2) and 40 nm (3) periodicity in the top, middle and bottom images, respectively.

When performing AFM measurements directly onto the antidot lattice, a similar uniformity of the lattice parameters is observed, consistent with the SEM results. However, the full depth of the QW cannot be measured, due to the broadness of the AFM tip, making it impossible to enter the tip inside the pores as presented in figure 3(b). The shape of the pores was therefore characterised with cross-section TEM carried out in a Fei Strata DB 235 Dual-Beam focus ion beam (FIB) system

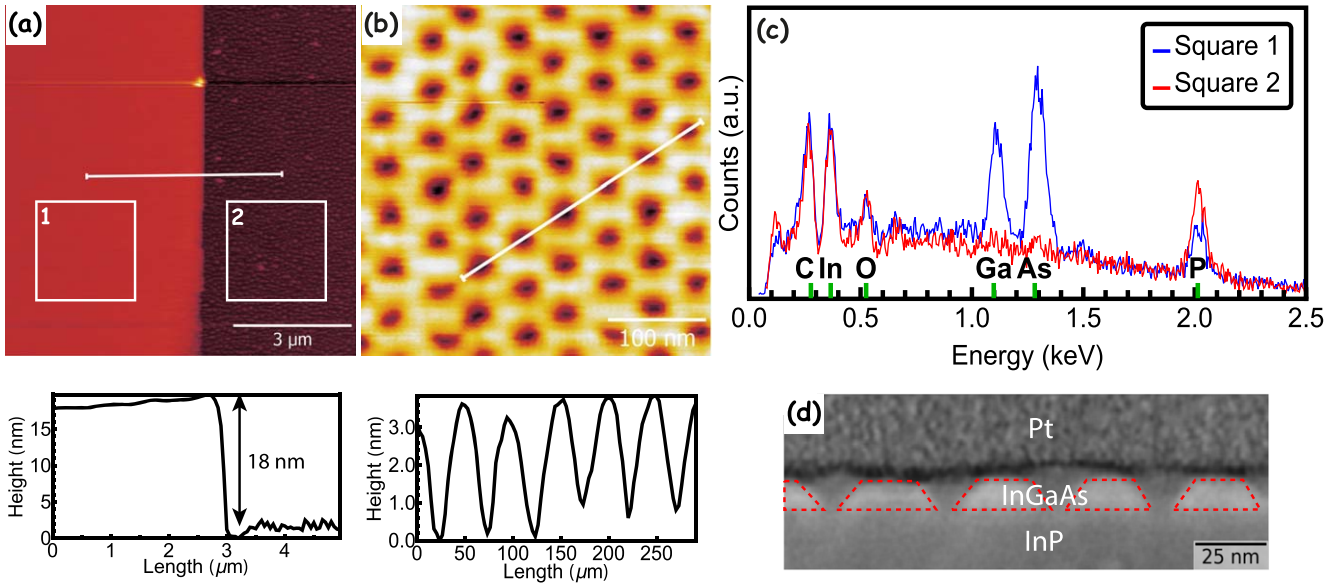

Figure 3. Structural and chemical characterisation of the nanoperforated InGaAs/InP heterostructure. (a) AFM image and height profile acquired along the horizontal direction. (b) AFM image of the nanoperforated InGaAs QW and height profile acquired along a tilted direction. (c) Chemical EDS analysis of the sample after ICP etching. The spectra were acquired in areas 1 and 2 defined in (a). (d) Cross-section scanning TEM image of the nanoperforated InGaAs/InP heterostructure, revealing the formation of conical pores instead of cylindrical pores.

operated at 30 kV equipped with a field emission gun. The spatial resolution was about 2 nm. The TEM foils were prepared by a FIB setup with Ga ions with a resolution of about 7 nm. The sample was protected by growing a layer of Pt on the top of the surface and a thin slice of the sample with a thickness of 200 nm is cut out.

The scanning TEM image of figure 3(d) shows the shape of the pores from the inner side. The pores have a conical shape instead of a cylindrical shape due to the non-perfect anisotropic etching process. However, the pores are fully etched down to the InP substrate.

2.3. Band structure calculations

In order to determine the band structure of the nanoperforated heterostructure, calculations were performed based on the geometry of the HC-SC material schematized in figures 4(a), (b). Muffin-tin (black) and tight binding (red) calculations of the band structure of a 10 nm thick InGaAs with a pore periodicity of 40 nm and pore radius r of 9.6 nm show a clear Dirac cone at the K point with an energy width of about 5.0 meV (figure 4(c)), due to coupling of the s-type on site envelope functions. The width is much larger with respect to the thermal energy of liquid helium (4.4 K, 0.38 meV), opening up the possibility to measure Dirac physics in lithography patterned heterostructures. At higher energies, we find a quasi flat band and a second Dirac cone due to coupling of the p-envelope functions. More details about the tight binding and the muffin-tin calculations can be found in the supplementary information (SI), available online at stacks.iop.org/NANO/30/155301/mmedia.

When decreasing the periodicity a of the antidot lattice, muffin-tin calculations show that the energy width of the Dirac cone increases according to $1/a^2$ (figure 4(d)), which is consistent with previous reports [10]. Since the pores are empty, they can be treated as hard repelling cylinders where the potential barrier of the pores is infinitely high. The relative size of the pore, defined by radius/periodicity, is kept constant in the calculation. When fixing the periodicity to 40 nm and varying the radius of the pores between very small (4 nm) to very large (16 nm), a maximal value of the energy width of the Dirac cone can be determined for an optimal pore radius (figure 4(e)). This maximum energy width can be found at a hole radius of approximately 8.5 nm, which gives an energy width of 5.3 meV.

The conical shape was taken into account in the tight-binding calculations for a periodicity of 40 nm and a pore radius of 14.2 nm (figure 4(f)). The radius of the pores was reduced from 100% on the top surface of the QW down to 20% at the bottom. The calculated band structure of such a type of sample is illustrated in figure 4(f). The band structure shows almost no change in the shape and energy width of the Dirac cone between the conical and cylindrical pores. Although the confinement effect will decrease when lowering the size of the pores further down, the coupling strength will increase. This interplay between the confinement effect and the coupling strength explains why the Dirac cone is only weakly affected by the conical shape of the pores. As a result, we can conclude that there is almost no negative effect to have conical pores over cylindrical pores on the Dirac band.

3. Effects of disorder in the DOS

The previous sections described the fabrication route of a 2D InGaAs semiconductor with a honeycomb geometry, and the

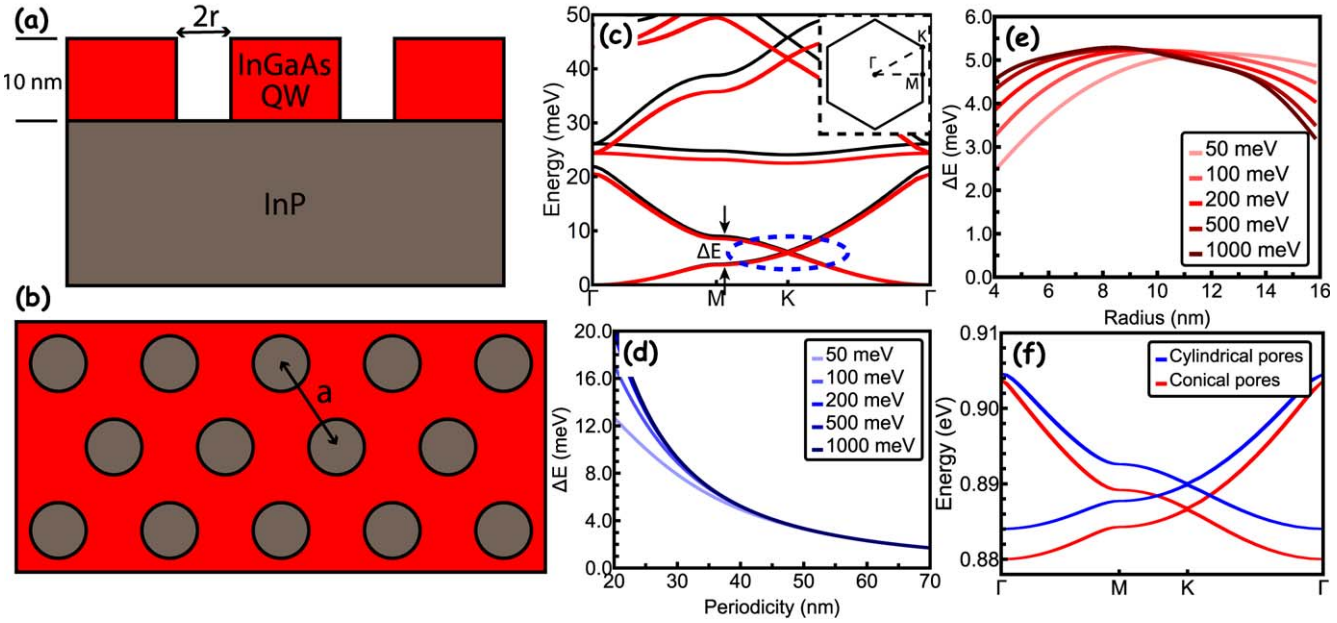

Figure 4. Schematic of the structure used to perform the muffin-tin and tight-binding calculations. (a), (b) Side and top view of a 10 nm InGaAs single crystal, 10 nm in thickness (red) with a triangular array of etched pores, thus forming a lattice inside the InGaAs/InP heterostructure. Critical structural parameters for the electronic band structure are the thickness of the InGaAs, here 10 nm, the radius r of the pores, and the periodicity, i.e. the distance between the centre of two adjacent pores corresponding to the unit cell constant a. (c) Conduction band structure for an InGaAs honeycomb lattice, with a periodicity a of 40 nm, a pore radius r of 9.6 nm and an electron repulsive potential of the pores of 1000 meV. The results of the muffin-tin calculations and tight-binding calculations are presented in black and red respectively. The bandwidth where the energy dispersion for the lowest Dirac cone is located is highlighted by a dotted ellipse. The width of the Dirac cone ΔE is defined as the energy difference of the first two bands at the M point. (d) Dirac cone width (taken at M) as a function of the honeycomb periodicity a. The size of the pores defined by the ratio r/a is kept constant. The calculations were performed for several repulsive potential values in the pores. (e) Dirac cone width (taken at M) as a function of the radius r of the pores for a fixed periodicity a of 40 nm. The calculations were performed for several values of the repulsive potential in the pores. (f) Tight binding calculations on conical pores (red) and cylindrical pores (blue) show that the Dirac cones in the band structures are almost unaltered with respect to each other.

resulting band structure. However, the robustness of the linear dispersion in the nanoperforated InGaAs quantum well is questionable. First, point defects and surface states exist and fluctuations of their charge states might disrupt the periodicity of the potential or cause a scattering of the charge carriers, reducing the carrier mobility and preventing the detection of Dirac cones in electrical measurements. High surface state densities could also make the direct observation of the local DOS in tunnelling spectroscopic measurements difficult. But previous experiments have shown that the step-like function of a quantum well DOS states can be probed for an InGaAs quantum well [24]. Moreover, treatments exist to efficiently passivate the surfaces of III–V semiconductors [25–27] and in particular the InGaAs(001) surface [28], so that the surface states become transparent to the tunnelling electrons in the energy range corresponding to energy levels of the quantum wells. However, even with a good passivation of the nanoperforated surfaces, other effects can significantly alter the band structure: a variation in the lattice constant (i.e. distance between pores), a variation in the radius of the pores and a variation in the shape of the pores. Among these three types of geometric variations, disorder in the periodicity should affect negatively the band structure, while variation in the 3D shape of the pore is expected to have a minor effect on the band structure (see e.g. the effect of the conical shape).

3.1. Particle detection script

We developed a particle detection protocol to quantify the disorder in the triangular antidot lattice, imaged by SEM. First, the quality of the image is improved by removing excessive number of pixels using Gaussian blurring. A black–white image of the SEM is obtained with an adaptive Gaussian threshold, making the pores detectable. All the pores are labelled, and small grains and hollows which are overlapping with the edge of the image are removed. The total number of pixels in the contour and area of each pore is detected, which is used to find the centre coordinates of each pore. The radius of each pore is calculated by fitting a perfect circle to every pore, and the circularity of each pore is determined using

$$C = \frac{4\pi A}{P^2}, \tag{1}$$

where A is the surface of the pore and P the perimeter of the pore. For a perfect round circle, this equation will yield one. The value C will go down when the pores are less round. Using the centre coordinates, all the nearest neighbour distances between the pores are computed. With the obtained data, we obtain three distributions that are plotted in histograms and fitted with a standard Gaussian distribution in order to determine their mean and the standard deviation. Using this particle detection script on the obtained SEM images, short

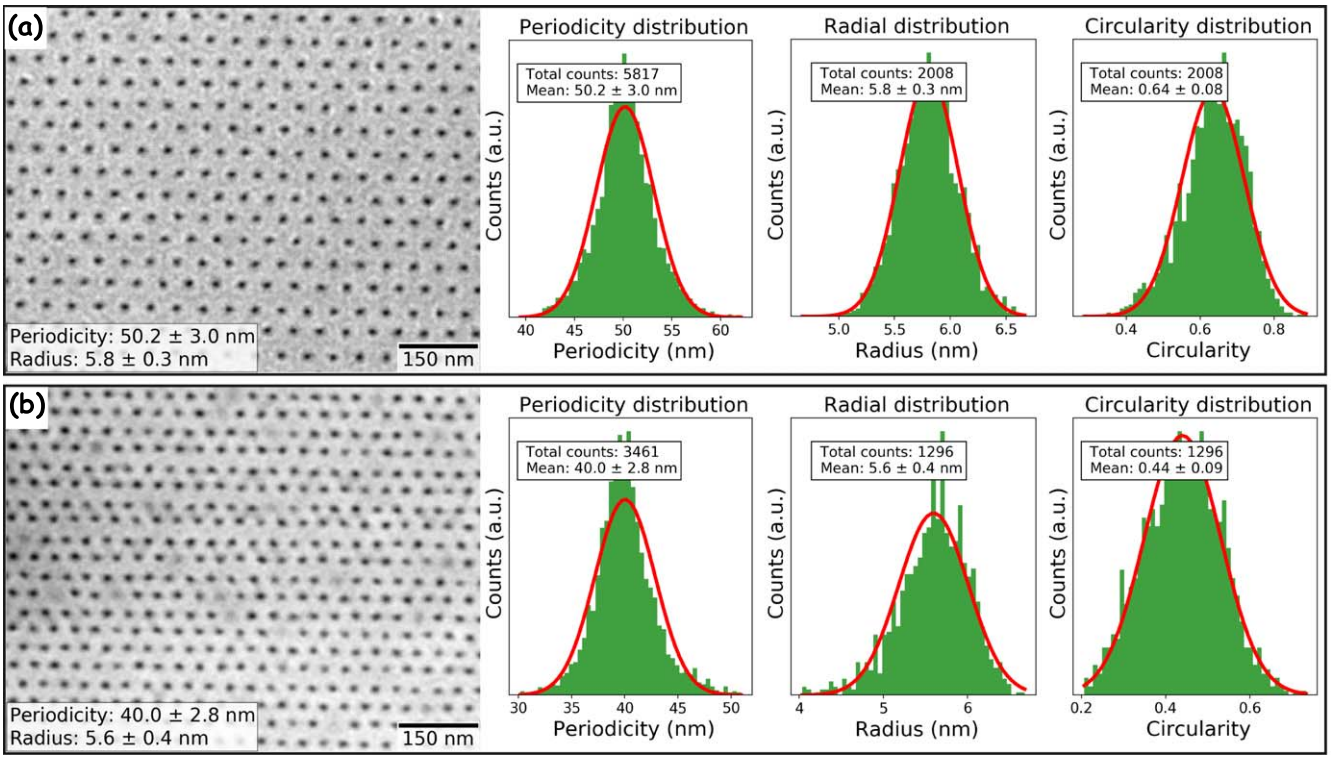

Figure 5. Analysis of the structural disorder parameters in a 2D honeycomb InGaAs sample with 50 nm (a) and 40 nm (b) periodicity. Distributions of the periodicity, pore radius and circularity are plotted next to the SEM images. The distributions are fitted with a standard Gaussian distribution. The total number of counts, the mean value and the standard deviation are indicated for each histogram.

range positional disorder and disorder in the shape of the pores can be immediately characterised.

The results of the particle detection script are presented in figure 5. For the 50 nm lattice (a), the calculated periodicity is 50.2 ± 3.0 nm with a pore radius of 5.8 ± 0.3 nm and a circularity of 0.64 ± 0.08. For the 40 nm lattice (b), the calculated periodicity yields 40.0 ± 2.8 nm with a pore radius of 5.6 ± 0.4 nm and a circularity of 0.44 ± 0.09, showing that the lattice constant in the 40 nm lattice is relatively more distorted than the 50 nm lattice, and the pores are less round than the pores in the 50 nm lattice.

3.2. Radial distribution function

For an accurate characterisation of long-range positional disorder inside the triangular antidot lattice, a 2D radial distribution function of the lattice is calculated to check if the disorder is completely random and independent of the disorder on other positions, or if any structural disorder is present in the lattice. A uniform disorder is obtained when the pore positions of a perfect lattice are displaced by a random displacement which is sampled from a Gaussian distribution. Conversely, a structural disorder is present when the disorder is not uniform. In order to discriminate whether the disorder is structural or random, the radial distribution function of the lattice can be fitted using two types of models: an ideal and a real paracrystal model [29, 30].

In an ideal paracrystal model, the spacing between two neighbouring lattice sites is generated by a variable D_i^{ideal} drawn from a Gaussian distribution with mean a and variance σ_{ideal} which does not depend on the positions of the other lattice sites. In this model, the variance of the distribution of the nth lattice site will be n times larger compared with the reference site, describing propagating disorder only.

The other model used for the analysis is the real paracrystal lattice. This model is generated by first creating an ideal paracrystalline lattice, and then shifting the lattice positions with an extra displacement D_i^{real} drawn from a Gaussian distribution with variance σ_{real}. When looking at the nth lattice site away from a reference point, the total variance of the distribution is a summation of σ_{ideal} which scales linearly with n, and σ_{real} which does not scale with n. Therefore, σ_{real} can describe the non-propagating disorder in the lattice. More information about the mathematical background of the two different models can be found in the SI.

The calculated radial distribution functions of the 50 and 40 nm antidot triangular lattices are fitted with both models, which are presented in figure 6. For both the 50 and 40 nm antidot lattices, the real paracrystalline model is a better fit than the ideal model, showing that random disorder dominates over structural disorder in both antidot lattices. For the 50 nm antidot lattice, the structural disorder term σ_{ideal} is 0.83 nm and the random disorder term σ_{real} is 2.15 nm. For the 40 nm antidot lattice, the structural disorder term is 1.02 nm and the random disorder term is 1.79 nm, showing that there is more random disorder in the 50 nm antidot lattice compared with the 40 nm one, and that there is more structural disorder in the 40 nm antidot lattice compared with the 50 nm one. This effect is highlighted in figures 6(c) and (f):

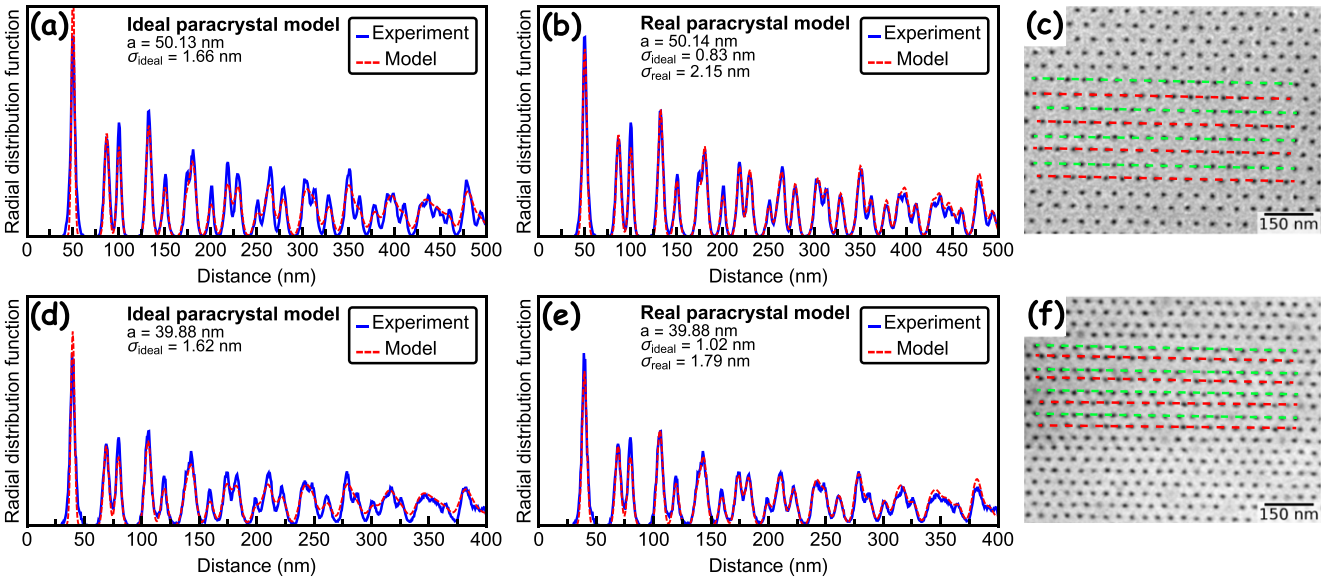

Figure 6. Order–disorder characterisation in two InGaAs triangular antidot lattices with periodicity of 50 and 40 nm. (a), (b), (d), (e) Radial distribution function for the InGaAs experimental lattice of 50 nm (a), (b) and 40 nm (d), (e) in blue fitted with a ideal paracrystalline model (a), (d) and a realistic paracrystalline model (b), (e) in red. (c), (f) SEM image of the InGaAs triangular antidot lattice with a periodicity of 50 nm (c) and 40 nm (f), including green and red dashed lines along the *x*-direction of the lattice. (c) The 50 nm lattice shows no visible propagating disorder in the *y*-direction, while (f) the 40 nm lattice show a clear structural disorder in the *y*-direction.

for the 50 nm antidot lattice, the distances between the pores stay visibly the same in the *y*-direction, while for the 40 nm antidot array the distances change alternately, indicating that a structural disorder is present inside the lattice. The origin of the structural disorder is still unknown, but different writing techniques [31] and different types or resist [32] for the EBL can be investigated to lower the structural disorder in the antidot lattice.

3.3. DOS calculations

The effect of the disorder inside the antidot lattices on the DOS can be calculated by distorting the on-site energy terms of the Hamiltonian, obtained from the muffin-tin calculations. First, a large super cell with $M \times M$ lattice sites is defined. The Hamiltonian of every k-mesh point inside the Brillouin zone framed by the high-symmetry lines $\Gamma \rightarrow K \rightarrow M \rightarrow \Gamma$ is calculated, and all the on-site energy terms $\mathcal{H}_{i,i}$ of the lattice sites of the unit cell are distorted with an energy term E^{dis}:

$$\mathcal{H}_{i,i}^{\mathrm{dis}} = \mathcal{H}_{i,i} + E^{\mathrm{dis}}. \tag{2}$$

Every separate energy term E^{dis} is determined by drawing a random value from a Gaussian distribution with mean 0 and a standard deviation σ_{dis}.

The energy disorder σ_{dis} calculated in the antidot lattice can be directly linked to the disorder obtained from the analysis on the antidot lattices by calculating several band structures with different periodicities while keeping the ratio r/a and potential constant. By varying the periodicity of the lattice, the height of the Dirac cone will change and the difference in energy height of the Dirac cone with respect to the 40 nm lattice can be calculated (figure 7(a)). For a disorder of 2.8 nm, an energy disorder between −1.5 and 2.0 meV is found, indicated by the dotted line. We note that this result is obtained for a pore radius of 5.6 nm. If the pore radius increases to 14 nm, a disorder of 2.8 nm implies an energy disorder of about 6 meV due to stronger particle confinement, which can possibly destroy the Dirac cone in the DOS (see supporting SI). Therefore, small pore sizes should be preferred as they cause less change in the DOS when the lattice is distorted. More information on the distorted DOS calculation can be found in the SI.

Results for a disordered lattice are presented in figure 7(b). This calculation is performed on a 24 × 24 lattice. For a perfect lattice, a straight V-like shape centred around 7 meV, signature of a perfect Dirac cone can be observed. The asymmetry of the DOS is caused by the interaction with the p states that are close to the s states due to the small radius of the pores. When adding disorder E^{dis} up to 2.5 meV to the on-site lattice site $\mathcal{H}_{i,i}$ consistent with the values deduced above, the presence of a Dirac cone in the DOS is still recognisable, although the magnitude of the V-shape is reduced and the apex of the V-shape less resolved.

4. Summary and conclusions

To summarise, a route has been described to create HC-SC samples in InGaAs/InP QW heterostructures which are perforated with a 2D triangular antidot lattice using EBL. Triangular antidot lattice with periodicities of the pores down to 40 nm have been demonstrated, giving an effective honeycomb lattice constant of 23 nm. The morphology of the samples is thoroughly studied by using various tools, revealing a good degree of control on the lattice parameters. At the smallest periodicity, muffin-tin and tight binding calculations show a clear Dirac cone at the K point with an

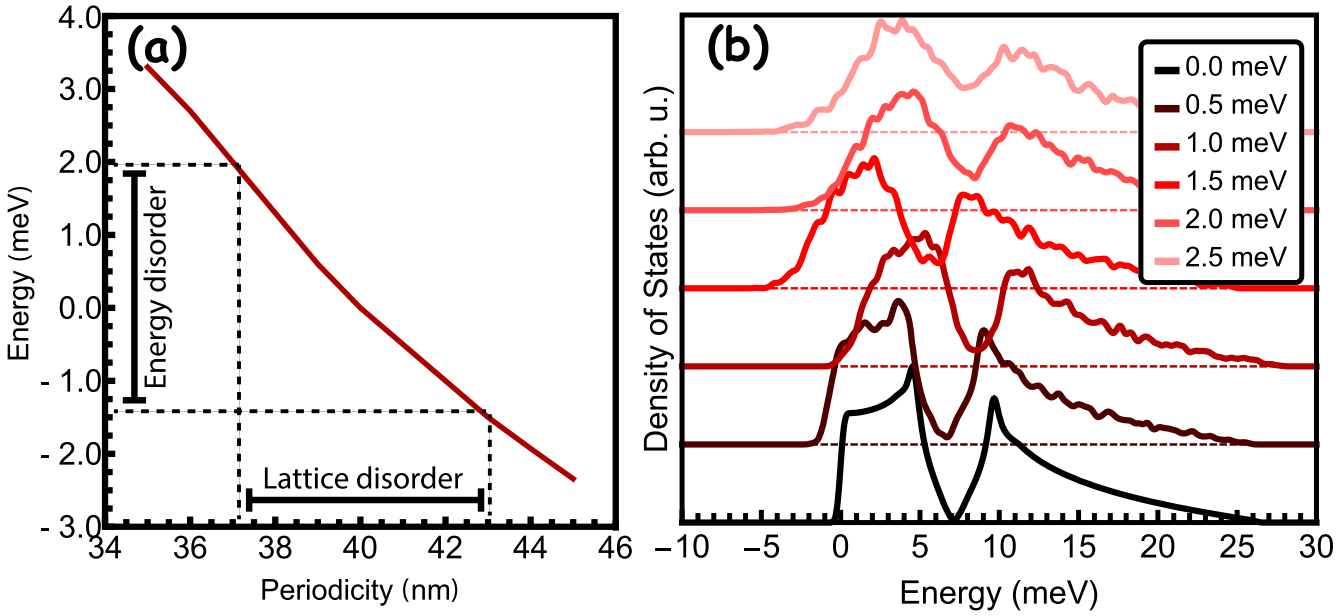

Figure 7. Density of states calculations for a perfect and a distorted 40 nm triangular antidot lattice inside an InGaAs QW with a potential height of 1000 meV and 2500 k-mesh points inside the Brillouin zone. (a) To determine the disorder energy term, the change in the energy height at the K point is calculated from the band structure for several periodicities around 40 nm. For a disorder of 2.8 nm, an energy disorder up to 2.0 meV is found. (b) Distorted DOS of the InGaAs triangular antidot lattice with random distorted energy terms with a variance of 0, 0.5, 1.0, 1.5, 2.0 and 2.5 meV. A clear Dirac cone can be observed for a perfect lattice, and it broadens but remains visible when adding more disorder to the calculation.

energy width of several meV. The disorder of the antidot lattices has been thoroughly studied using an effective particle detection protocol and by calculating the radial distribution function of the antidot lattices. Two different models have been considered to discriminate between random and structural disorder in the antidot lattice. Although both types of disorder exist in the antidot lattice with a periodicity of 40 nm, theoretical calculations of the DOS have revealed that the signature of the Dirac cone survives to the fluctuations of the pore periodicity and sizes that were measured. Because lattice disorder is inherent in structures prepared with EBL at the ultimate resolution, our results provide general guidelines to be able to probe Dirac cones in HC-SC consisting of III–V heterostructures. The next step is to passivate the surface of the nanostructured QW by using wet chemical passivation methods to suppress surface states and surface defects. Other methods, such as regrowth processes used in selective area epitaxy [33–35] could also be applied to improve the electronic quality of the HC-SC.

Acknowledgments

This work was financially supported by the Netherlands Organisation for Scientific Research (Grant No. BC.000672.1, TOP Punt), the National Natural Scientific Foundation of China (Grant No. 61775130), the French National Research Agency (Dirac III-V project ANR-16-CE24-0007-01), the French state funds managed by the ANR within the Investissements d'Avenir programme EQUIPEX Excelsior (ANR-11-EQPX-0015) and the RENATECH network.

ORCID iDs

L C Post https://orcid.org/0000-0001-9271-7225
T Xu https://orcid.org/0000-0003-1410-9261
L Desplanque https://orcid.org/0000-0002-2197-4408
B Grandidier https://orcid.org/0000-0001-6131-7309

References

[1] Tadjine A, Allan G and Delerue C 2016 *Phys. Rev.* B **94** 075441
[2] Polini M, Guinea F, Lewenstein M, Manoharan H C and Pellegrini V 2013 *Nat. Nanotechnol.* **8** 625–33
[3] Kalesaki E, Delerue C, Morais Smith C, Beugeling W, Allan G and Vanmaekelbergh D 2014 *Phys. Rev.* X **4** 011010
[4] Du X, Skachko I, Duerr F, Luican A and Andrei E Y 2009 *Nature* **462** 192–5
[5] Bolotin K I, Ghahari F, Shulman M D, Stormer H L and Kim P 2009 *Nature* **462** 196–9
[6] Novoselov K S, Geim A K, Morozov S V, Jiang D, Katsnelson M I, Grigorieva I V, Dubonos S V and Firsov A A 2005 *Nature* **438** 197–200
[7] Boneschanscher M P *et al* 2014 *Science* **344** 1377–80
[8] Geuchies J J *et al* 2016 *Nat. Mater.* **15** 1248–54
[9] Delerue C and Vanmaekelbergh D 2015 *2D Mater.* **2** 034008
[10] Gibertini M, Singha A, Pellegrini V, Polini M, Vignale G, Pinczuk A, Pfeiffer L N and West K W 2009 *Phys. Rev.* B **79** 241406

[11] Park C H and Louie S G 2009 *Nano Lett.* **9** 1793–7
[12] Nádvorník L *et al* 2012 *New J. Phys.* **14** 053002
[13] De Simoni G, Singha A, Gibertini M, Karmakar B, Polini M, Piazza V, Pfeiffer L N, West K W, Beltram F and Pellegrini V 2010 *Appl. Phys. Lett.* **97** 132113
[14] Singha A *et al* 2011 *Science* **332** 1176–9
[15] Wang S *et al* 2018 *Nat. Nanotechnol.* **13** 29–33
[16] Du L *et al* 2018 *Nat. Commun.* **9** 3299
[17] Yuzeeva N A, Sorokoumova A V, Lunin R A, Oveshnikov L N, Galiev G B, Klimov E A, Lavruchin D V and Kulbachinskii V A 2016 *J. Low Temp. Phys.* **185** 701–6
[18] Wallart X, Pinsard B and Mollot F 2005 *J. Appl. Phys.* **97** 053706
[19] Millunchick J, Riposan A, Dall B, Pearson C and Orr B 2003 Surface reconstructions of InGaAs layers *2003 Int. Symp. on Compound Semiconductors* (IEEE: Piscataway, NJ) pp 43–4
[20] Li H, Wu J, Wang Z, Liang J, Xu B, Jiang C, Gong Q, Liu F and Zhou W 1998 *J. Cryst. Growth* **186** 309–14
[21] Flindt C, Mortensen N A and Jauho A P 2005 *Nano Lett.* **5** 2515–8
[22] Xu T *et al* 2018 *Nanoscale* **10** 7519–25
[23] Maeda T, Cho H, Hong J and Pearton S J 1999 *J. Electron. Mater.* **28** 118–23
[24] Perraud S, Kanisawa K, Wang Z Z and Hirayama Y 2006 *Appl. Phys. Lett.* **89** 192110
[25] van Vugt L K, Veen S J, Bakkers E P A M, Roest A L and Vanmaekelbergh D 2005 *J. Am. Chem. Soc.* **127** 12357–62
[26] Durand C, Berthe M, Makoudi Y, Nys J P, Leturcq R, Caroff P and Grandidier B 2013 *Nanotechnology* **24** 275706
[27] Nadar S, Rolland C, Lampin J F, Wallart X, Caroff P and Leturcq R 2015 *Nano Res.* **8** 980–9
[28] Melitz W, Kent T, Kummel A C, Droopad R, Holland M and Thayne I 2012 *J. Chem. Phys.* **136** 154706
[29] Savitzky B H, Hovden R, Whitham K, Yang J, Wise F, Hanrath T and Kourkoutis L F 2016 *Nano Lett.* **16** 5714–8
[30] Whitham K, Yang J, Savitzky B H, Kourkoutis L F, Wise F and Hanrath T 2016 *Nat. Mater.* **15** 557–63
[31] Trasobares J, Vaurette F, François M, Romijn H, Codron J L, Vuillaume D, Théron D and Clément N 2014 *Beilstein J. Nanotechnol.* **5** 1918–25
[32] Okazaki S 2015 *Microelectron. Eng.* **133** 23–35
[33] Fahed M, Desplanque L, Troadec D, Patriarche G and Wallart X 2016 *Nanotechnology* **27** 505301
[34] Desplanque L, Bucamp A, Troadec D, Patriarche G and Wallart X 2018 *Nanotechnology* **29** 305705
[35] Pastorek M *et al* 2019 *Nanotechnology* **30** 035301